Insights into Capillary-Driven Motion of Micro-Particles Interacting with Advancing Meniscus on Substrate

Muhammad Sajjad[a,c], Hongxia Li[a], Aikifa Raza[a], Faisal AlMarzooqi[b], TieJun Zhang[a]*

[a] Department of Mechanical Engineering, Masdar Institute, Khalifa University of Science and Technology, P. O. Box 127788, Abu Dhabi, UAE

[b] Department of Chemical Engineering, Masdar Institute, Khalifa University of Science and Technology, P. O. Box 127788, Abu Dhabi, UAE

[c] Department of Mechanical Engineering, Khwaja Fareed University of Engineering and Information Technology, Rahim Yar Khan, P. O. Box 64200, Pakistan

*Address correspondence to: tiejun.zhang@ku.ac.ae

S1. Controlling dynamic contact angle of the air-liquid-substrate contact line

The dynamic contact angle was varied by adjusting two parameters: (i) ratio of spreading length (L) of the air-liquid-substrate contact line to the width of the channel (W) as shown in Fig. S1 and (ii) separation distance between the micro-particle and air-liquid-substrate contact line (S) as shown in Fig. S1. As the dimensions of the channel were fixed (with W=5 mm), the ratio L/W depends on the volume of the droplet (i.e., small puddle) which can be controlled by the amount of liquid added to the existing droplet through discrete small drops. Interaction at higher air-liquid-substrate dynamic contact angles (i.e., > 80 °) was achieved either by keeping the L/W ratio below ½ or placing the micro-particle at a separation distance lower than ~ 100 μm. To achieve interaction at a lower dynamic contact angle (<80 °), the particle was placed at a separation distance greater than ~ 200 μm with L/W >1/2. It is due to the fact that the velocity of the advancing meniscus gradually reduces as it advances over the substrate which results in a low dynamic contact angle at the onset of interaction. Moreover, the increase in spreading length (ΔL) will be higher for the case with L/W <1/2 compared to the case when L/W >1/2 (Fig. S1). There may be some cases where pinning of the air-liquid-substrate (ALS) contact line results in a higher dynamic contact angle even though L/W >1/2 and the particle is placed at a separation distance greater than ~200 μm.

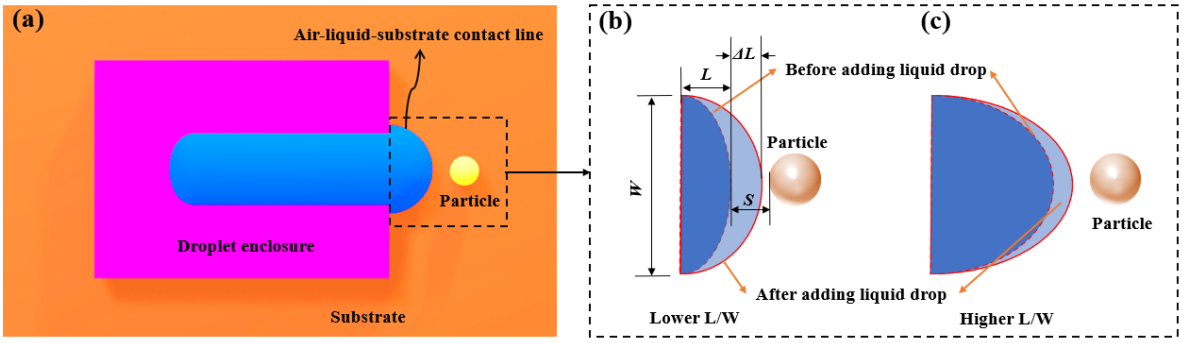

Fig. S1. (a) Schematic of the experimental setup to generate and advance air-liquid-substrate (ALS) contact line. (b)-(c) Effect of L/W ratio (spreading length of air-liquid-substrate contact line to the width of the channel) and S (separation distance between the micro-particle and advancing meniscus) on dynamics of the advancing meniscus at the onset of interaction.

S2. Variation in dynamic contact angle of the air-liquid-substrate contact line

The variation in the dynamic contact angle of the air-liquid-substrate contact line (β_d as sketched in the inset optical image) before its interaction with a soda lime glass micro-particle is shown in Fig. S2. The time t=0 refers to the instant when the interaction between air-liquid-substrate and micro-particle commences.

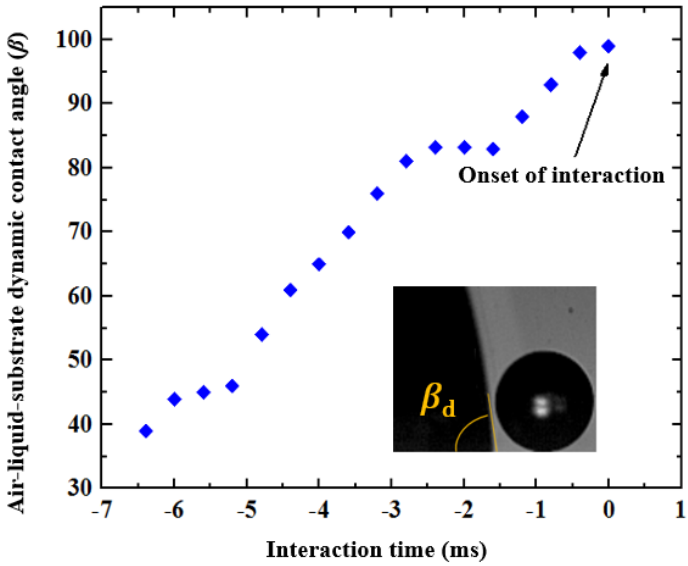

Fig. S2. Variation in dynamic contact angle of the advancing air-liquid-substrate contact line.

The advancing air-liquid-particle contact line with moving (a) and pinned (b) triple points is shown with a solid blue curve in Fig. S3. To compute contact line velocity (u_{ALS}), the distance covered by the air-liquid interface (Δx) was measured parallel to the center line of the micro-particle. The corresponding time interval (Δt) for the calculation of u_{ALS} was 800 μs before the commencement of interaction.

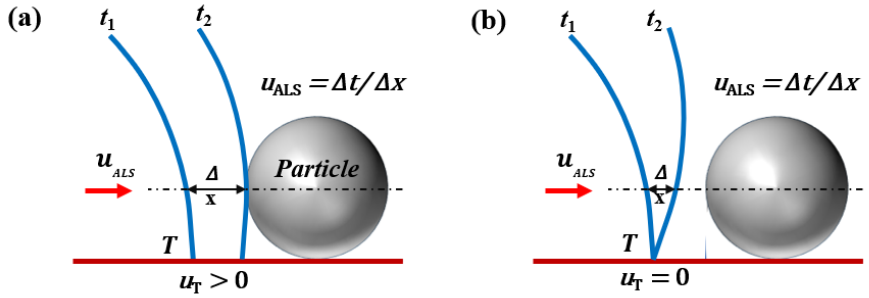

Fig. S3. Side view schematic of the advancing contact line (shown with a solid blue curve) with moving (a) and pinned (b) triple points. The u_{ALS} and u_T are the velocities of the air-liquid-substrate contact line and triple point, respectively.

S3. Interfacial energy analysis

The capillary forces arise owing to changes in interfacial energy of the air-liquid-particle-substrate system. Therefore, the interaction mechanism can be explained through the energy argument in addition to the force argument considered in the main text. The change in total interfacial energy (E) of the air-water-particle-substrate system is given by Eq. S1.

$$\Delta E = \sigma_l \left(dA_{l-g} + dA_{l-p} \cos\theta_{E,l-p} + dA_{l-s} \cos\theta_{E,l-s} \right) \tag{S1}$$

The first, second and third terms on the right side of Eq. (S1) are related to changes in interfacial energies of the liquid-gas, liquid-particle and liquid-substrate interfaces, respectively. The subscripts l, g, p, s represent liquid, gas (i.e. air), micro-particle and substrate, respectively, while symbols σ_l, A and θ_E represent surface tension, interfacial area and equilibrium contact angle, respectively. The change in surface energy of the liquid-substrate interface is negligible compared to that of liquid-gas and liquid-particle interfaces ($|dA_{l-s}| << |dA_{l-p}|$ and $|dA_{l-s}| << |dA_{l-g}|$) for at least

t < 560 μs as shown in Fig. 3b in the main text. Therefore, for the initial period of t < 560 μs, the change in surface energies of the liquid-gas and liquid-particle interfaces will result in forces which will only act on the particle as given by Eq. (S1). When the air-liquid-particle (ALP) contact line advances along the surface of the micro-particle, the change in surface energy of the air-liquid-particle system will be negative and net positive force will act on the particle. However, as discussed in the main manuscript, the inward-moving particle will push and drag the air-liquid-particle contact line back and the corresponding change in surface energy of the system will become positive. The interfacial energy of the system will increase at the expense of the particle's inertial energy.

S4. Theoretical modelling

S4.1 Forces governing the interaction

The forces which govern the capillary-driven motion of the micro-particle are surface tension force (F_σ), Laplace pressure force (F_{LP}), drag force (F_D) and frictional force (F_f) between particle and substrate are shown in Fig. S4. At any point along the air-liquid-particle (ALP) contact line, the reaction of the surface tension force ($F_{xy\text{-}\sigma}$) will have two components as given by Eqs. (S2)-(S3).

Along x-axis:

$$F_{x-\sigma} = 2\pi\sigma_l R_p \sin\phi \sin\left(\theta_d + \phi\right) \tag{S2}$$

Along y-axis:

$$F_{y-\sigma} = -2\pi\sigma_l R_p \sin\phi \cos\left(\theta_d + \phi\right) \tag{S3}$$

The symbol θ_d, ϕ, σ_l and R_p represents the dynamic contact angle of the air-liquid-particle contact line, filling angle, liquid surface tension and particle radius, respectively. Laplace pressure force can be expressed in terms of the mean radius of curvature (R_m) as:

$$F_{LP} = \frac{2\pi\sigma {R_p}^2 \sin^2\phi}{R_m} \tag{S4}$$

The mean radius of curvature (R_m) can be computed as:

$$\frac{1}{R_m} = \frac{1}{2}\left(\frac{1}{R_1} + \frac{1}{R_2}\right) \tag{S5}$$

where R_1 and R_2 are the two principal radii used in the computation of Laplace Pressure force. The correlation for R_1 derived by Orr et. al. [1] for pendular rings between spherical particles is given as:

$$R_1 = \frac{R_p \sin\phi}{\sin(\theta+\phi)} \tag{S6}$$

R_2 depend on the profile and curvature of the air-liquid-particle contact line. By assuming a straight air-liquid interface ($R_2 \to \infty$) at the air-liquid-particle contact line and substituting the correlation for R_1 from Eq. (S6) into Eq. (S7):

$$\frac{1}{R_m} = \frac{1}{2}\left(\frac{\sin(\theta+\phi)}{R_p \sin\phi}\right) \tag{S7}$$

Substituting correlation of mean radius (R_m) given in Eq. (S7) into Eq. (S4):

$$F_{LP} = \pi\sigma R_p \sin\phi \sin(\theta+\phi) \tag{S8}$$

Eq. (S8) shows that the Laplace pressure force is half of the surface tension force for a straight air-liquid interface ($R_2 \to \infty$) at the air-liquid-particle contact line.

Frictional force during sliding ($F_f = \mu_k N$) depends on the smoothness of the substrate and surface normal force (N) at the contact point between the substrate and micro-particle. The symbol μ_k represents the coefficient of sliding friction. The drag force (F_D) on the particle can be expressed as a function of drag coefficient (C_D), frontal area (A_f), and particle's relative velocity ($u_{p\text{-}rel}$) as:

$$F_D = C_D A_f \rho_l {u_{p-rel}}^2 / 2 \tag{S9}$$

The drag coefficient depends on the flow Reynolds number $Re = \rho_l u_{p\text{-}rel} D_p / \eta$. The symbol ρ_l, $u_{p\text{-}rel}$, D_p and η represents the density of the liquid, the relative velocity of the particle, the particle diameter and the viscosity of the liquid, respectively. The drag coefficient can be modeled

through Stokes′ law ($C_D = 24/\mathrm{Re}$, Re <1) or by a more general correlation given by Clift and Gauvin [2].

$$C_D = \frac{24}{\mathrm{Re}}\left(1 + 0.15\,\mathrm{Re}^{0.687}\right) + \frac{0.42}{1 + 4.25\times10^{4}\,\mathrm{Re}^{-1.16}} \tag{S10}$$

The rate of change of momentum of the sliding micro-particle can be written as:

$$m_p \vec{u}_p = \vec{F}_{x-\sigma} - \vec{F}_{LP} - \vec{F}_D - \vec{F}_f \tag{S11}$$

By introducing dimensionless parameters such as equivalent capillary-inertial velocity ($u_{c,E} = \sqrt{\sigma/\rho_p R_p}$), equivalent capillary-inertial time ($t_{c,E} = R_p/u_{c,E}$), capillary number ($Ca = \eta u_{p-rel}/\sigma_l$), radii ratio parameter ($r_k = R_p/R_m$), and equivalent Bond number ($B_{o,E} = \rho_p g R_p^2/\sigma_l$), the rate of change of momentum of the particle can be re-written in non-dimensionalized form as given by Eq. (S12).

$$\frac{du_p^*}{dt^*} = \frac{3}{2}\left(\sin\phi\cos\alpha - r_k\sin^2\phi - \frac{1}{8}\mathrm{Re}\,Ca C_D \sin^2\phi' - \frac{2}{3}\mu_f B_{o,E}\right) \tag{S12}$$

Substituting radii ratio parameter $r_k = R_p/R_m$ into Eq. (S12):

$$\frac{du_p^*}{dt^*} = \frac{3}{2}\left(\sin\phi\cos\alpha - \frac{R_p}{R_m}\sin^2\phi - \frac{1}{8}\mathrm{Re}\,Ca C_D \sin^2\phi' - \frac{2}{3}\mu_f B_{o,E}\right) \tag{S13}$$

Substituting mean radius (R_m) from Eq. (S7) into Eq. (S13) and setting $\alpha = \theta_d + \phi - \frac{\pi}{2}$:

$$\frac{du_p^*}{dt^*} = \frac{3}{2}\left(\frac{1}{2}\sin\phi\cos\alpha - \frac{1}{8}\mathrm{Re}\,Ca C_D \sin^2\phi' - \frac{2}{3}\mu_f B_{o,E}\right) \tag{S14}$$

Setting $\frac{du_p^*}{dt^*}$ =0 to find maximum velocity while neglecting frictional force:

$$\sin\phi\cos\alpha = \left(\frac{1}{4}\mathrm{Re}\,Ca C_D \sin^2\phi'\right) \tag{S15}$$

Substituting values of Reynolds number (Re), capillary number (Ca) and equivalent capillary-inertial velocity ($u_{c,E}$):

$$\sin\phi\cos\alpha = \left(\frac{1}{2}\rho_l \frac{u^2{}_{p-rel}}{\sigma_l} R_p C_D \sin^2\phi'\right) \tag{S16}$$

The filling angle for drag force is $\phi' = \phi$ for $\phi \le \pi/2$ and $\phi' = \pi/2$ for $\phi > \pi/2$. Assuming peak velocity happens at $\phi \le \pi/2$:

$$u^2{}_{p-rel} = 2\cos\alpha\left(\frac{\sigma_l}{R_p\rho_l}\right)\frac{1}{C_D\sin\phi} \tag{S17}$$

From Eq. (S17), the maximum velocity of the particle ($u'_{p-rel} = u_{p-rel}/u_c$) normalized with capillary-inertial velocity ($u_c = \sqrt{\sigma_l/\rho_l R_p}$) can be written as:

$$u'_{p\text{-rel,max}} = \sqrt{\frac{2}{C_D}\frac{\cos\alpha}{\sin\phi}} \tag{S18}$$

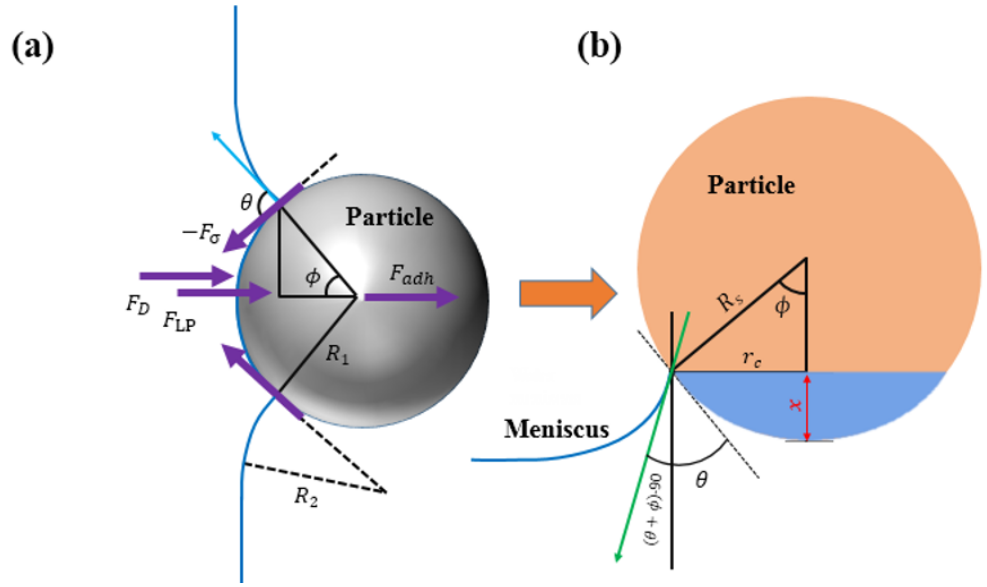

Fig. S4. (a) Illustration of various forces governing the ballistic-like motion of a micro-particle. (b) Geometric representation of kinematic features of air-liquid-particle contact line (viewed from the top)

S4.2 Numerical solution

Eq. 1 was numerically solved using the ode45 function of MATLAB. For dynamic contact angle (θ_d) and filling angle (ϕ), empirical data given in Fig. 3d-e in the main text was employed. The discrete experimental data for θ_d and ϕ was interpolated using the linear spline interpolation function of MATLAB. The kinetic coefficient of friction for glass-glass contact was taken as 0.4 [3]. The density, dynamic viscosity and surface tension of the water were taken as 997 kg/m^3, 0.00089 Ns/m^2 and 0.072 N/m, respectively.

S4.3 Relative velocity, drag coefficient and drag force

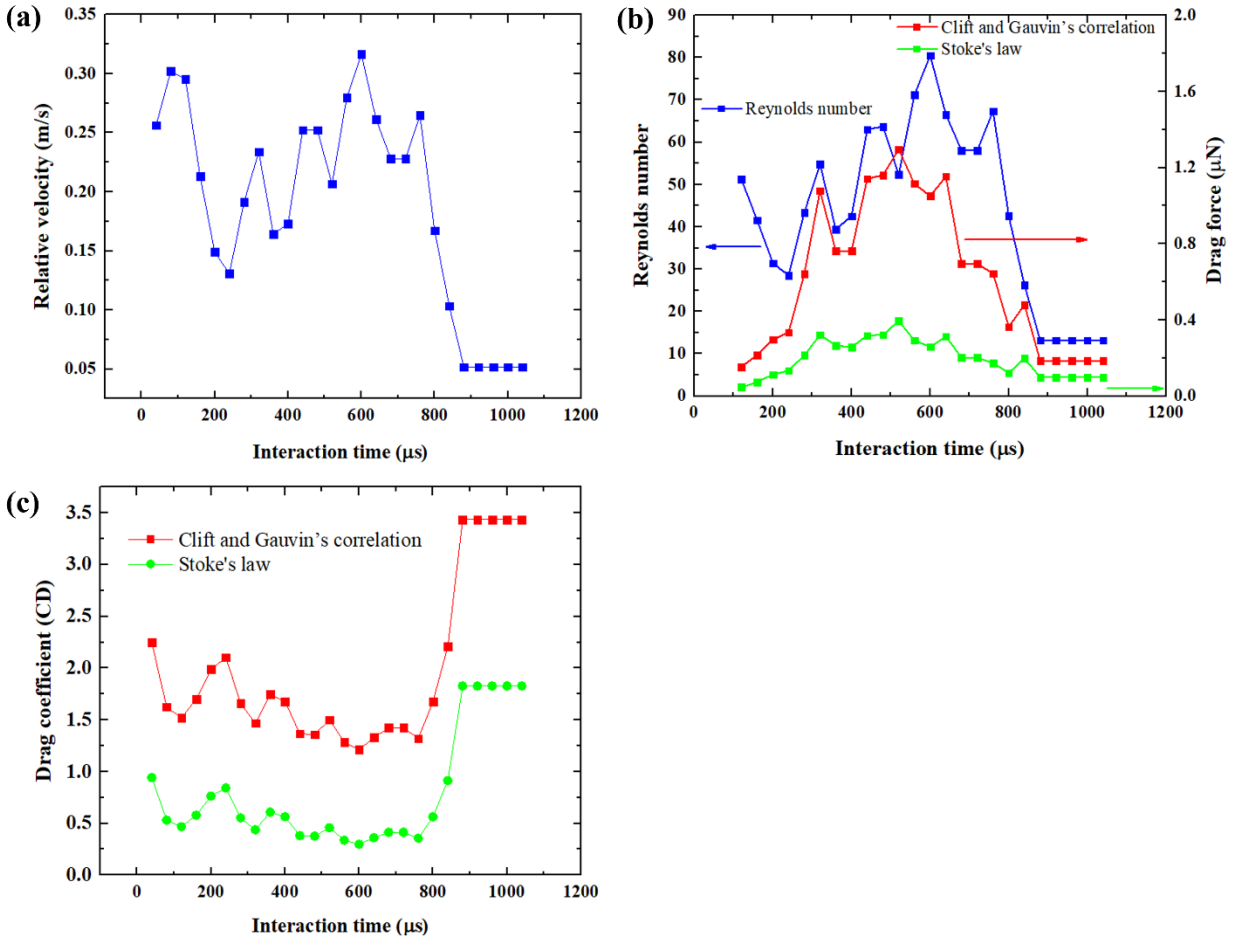

Fig. S5. (a) Relative velocity of the particle as a function of interaction time, (b) Variation in Reynolds number and drag force with the interaction time (c) Drag coefficient as a function of interaction time modeled through Stoke´s law and Clift and Gauvin's correlation [2].

S4.4 Potential image artefacts in top-view imaging

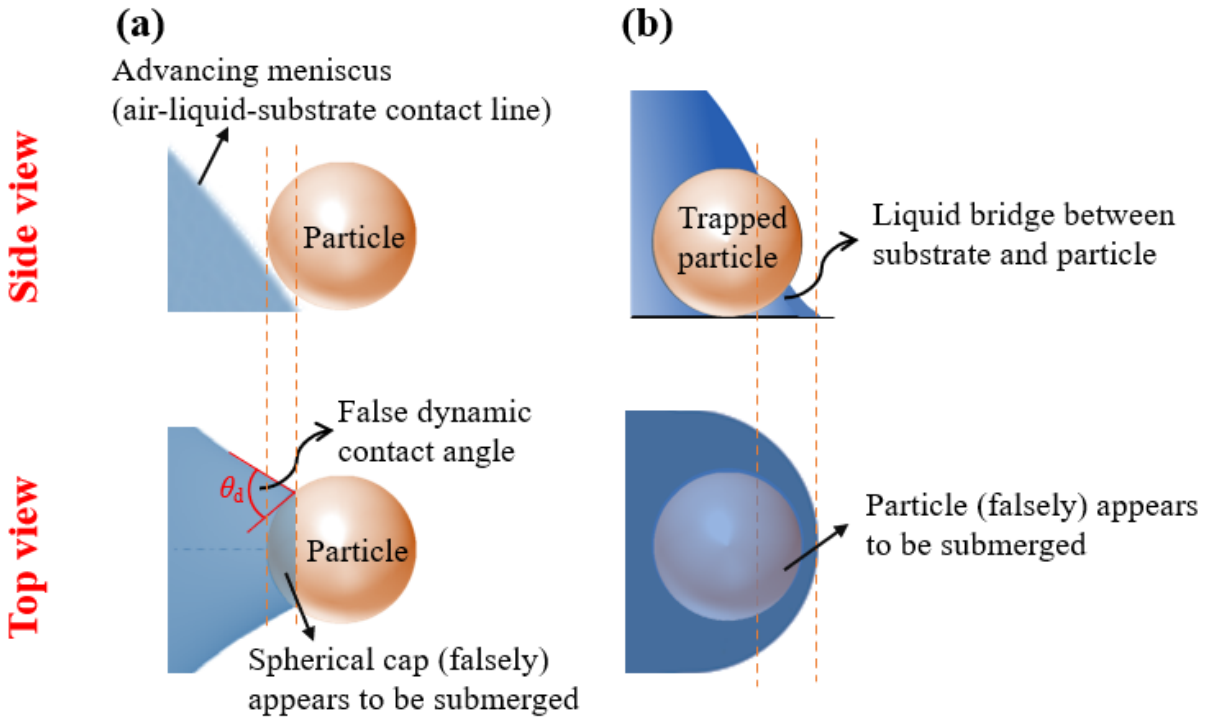

Fig. S6. Potential image artefacts in top view high-speed optical imaging

S5. Effect of particle type and liquid's surface tension

Related to Fig. 4b in the main text, the particle size (D_p), dynamic contact angle (β_d) and advancing velocity (u_{ASL}) of the air-liquid-substrate contact line and maximum absolute velocities ($u_{p,max}$) of the individual particles are given in Table S1 and S2 for polyethylene and soda lime glass micro-particles, respectively.

Table S1 (Polyethylene micro-particles)

Interaction no.	D_p (µm)	$u_{p,max}$ (m/s)	β_d	u_{ALS} (m/s)

1	216	0.1548	86	~ 0
2	210	0.1548	93	~ 0
3	218	0.2065	86	~ 0
4	230	0.1548	96	0.0154

Table S2 (Soda-lime glass micro-particles)

Interaction no.	D_p **(µm)**	$u_{p,max}$**(m/s)**	β_d	u_{ALS} **(m/s)**
1	200	0.256	86	~ 0
2	215	0.256	87	~ 0
3	223	0.20	87	0.0196
4	228	0.21	96	0.0309

Related to the results shown in Fig. 4e-f in the main text, Fig. S7 shows translational displacement of the soda lime glass micro-particle for the complete duration of capillary-driven motion (i.e. 254 ms).

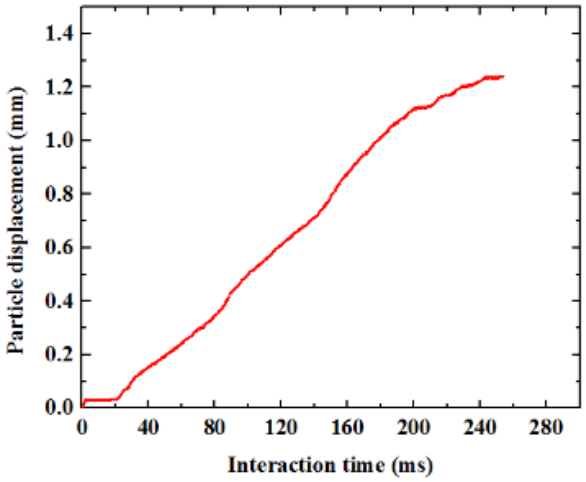

Fig. S7. Translational displacement of the soda lime glass micro-particle with a diameter of ~280 µm interacting with air-ethanol-substrate contact line

S6. Effect of particle size on the interaction mechanism

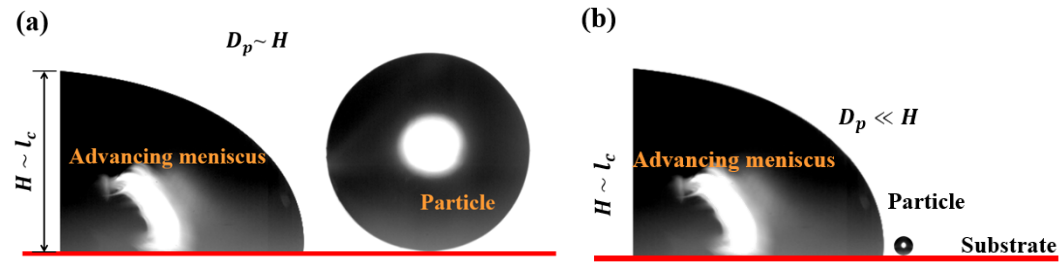

Fig. S8. (a) Interaction of advancing meniscus with a particle with its diameter (a) comparable to capillary length (i.e. $D_p \sim l_c$) and with a particle with its diameter (b) sufficiently smaller than capillary length (i.e. $D_p << l_c$)

S7. Surface morphology of micro-particles

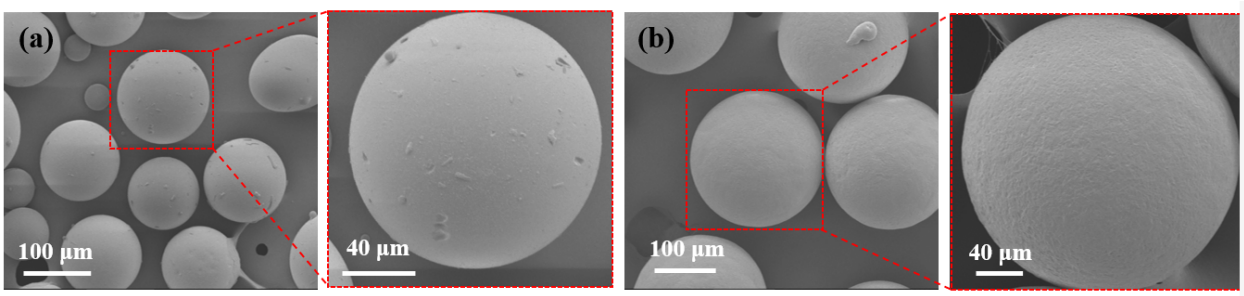

Fig. S9 Surface morphology of the (a) soda lime glass and (b) polyethylene micro-particles observed under Scanning Electron Microscopy (SEM, JEOL 7610)

S8 Zeta potential measurements

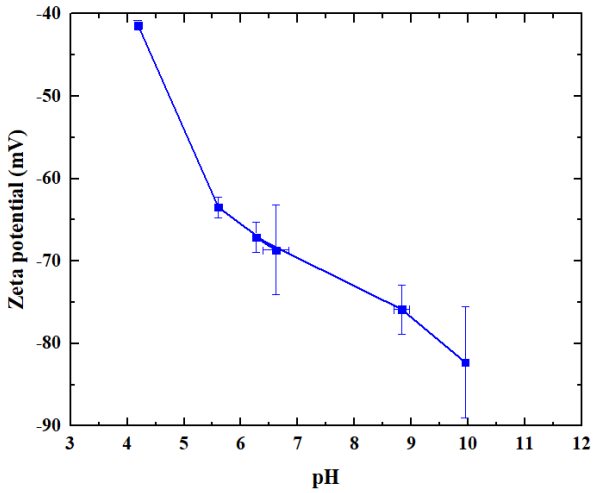

Fig. S10 Variation in the zeta potential of the hydrophilic glass substrate as a function of pH

S9 Derivation details for Eq. (3) given in the main text

If substrate-particle adhesive resistance is negligible, the capillary-driven motion will happen once the net capillary force is larger than the meniscus drag force acting on the particle. Based on Eq. (1) given in the main text, the following criterion (C-I) needs to be satisfied for the capillary-driven motion to happen:

$$F_c > F_D \tag{S19}$$

where F_c is net capillary force and F_D is drag force due to meniscus velocity. F_c can be calculated by substituting the values of $F_{x\text{-}\sigma}$ and F_{LP} from Eqs. (S2) and (S8) into $F_c = F_{x-\sigma} - F_{LP}$.

Substituting the value of F_c and drag force from Eq. (S9):

$$\pi\sigma R_p \sin\phi \sin\left(\theta_d + \phi\right) > C_D A_f \rho_l {u_p}^2 \big/ 2 \tag{S20}$$

Rearranging and introducing the meniscus (i.e. air-liquid-particle contact line) Weber number ($We_{ALP} = \rho_l u_{ALP} D_p \big/ \sigma_l$), the above expression can be re-written as:

$$4\left(\frac{\sin(\theta_d + \phi}{\sin\phi}\right) > We_{ALP}\ C_D \tag{S21}$$

The Weber number and the drag coefficient (C_D) are computed based on the velocity of the air-liquid-particle contact line.

S10 Criterion for capillary-driven motion

For impeding motion of a particle (while assuming that the interaction happens at a dynamic contact angle of $\pi/2$), Eq. (1) given in the main text can be modified as:

$$0 = \vec{F}_{x-\sigma} - \vec{F}_{LP} - \vec{F}_D - \vec{F}_f \tag{S22}$$

where $F_{x\text{-}\sigma}$ is surface tension force, F_{LP} is Laplace pressure force, F_D is drag force and F_f is static friction force, respectively. The particle will move only if the following criterion (C-II) is satisfied:

$$\vec{F}_{x-\sigma} - \vec{F}_{LP} - \vec{F}_D > \vec{F}_f \tag{S23}$$

The magnitude of the drag force is small compared to the capillary forces as observed from the results given in Fig. 3e in the main text and Fig. S5. Thus, the drag force due to meniscus velocity is not neglected. Though it will slightly overpredict the critical radius, the resulting criteria can be evaluated more conveniently. Therefore, the expression given in Eq. (S23) can be modified as:

$$\vec{F}_{x-\sigma} - \vec{F}_{LP} > \vec{F}_f \tag{S24}$$

Substituting the values of $F_{x\text{-}\sigma}$ and F_{LP} from Eq. (S2) and Eq. (S8), respectively and friction force ($F_f = \mu_s N = \mu_s W_p$) into Eq. (S24):

$$\pi\sigma_l R_p \sin\phi \sin\left(\theta_d + \phi\right) > \mu_s W_p \tag{S25}$$

Where μ_s is the coefficient of static friction and W_p is the particle weight. Rearranging and introducing equivalent Bond number ($B_{o,\,E} = \dfrac{\rho_b g D_p^2}{4\sigma_l}$), the above expression can be re-written as:

$$\mu_s B_{o,\,E} < \frac{3}{4}\left(\sin\phi \sin(\theta_d + \phi)\right)_{max} \tag{S26}$$

The symbols ρ_b, D_p, and μ_s represent the micro-particle density and its diameter and static friction coefficient. θ_d and ϕ are dynamic contact angle and filling angle of the air-liquid-particle contact line corresponding to the maximum net capillary force (F_c). Here the equivalent bond number quantifies the relative strength of friction force (as it depends on g) and capillary force. The expression given in Eq. (S26) provides a critical value for the product of equivalent Bond number and coefficient of static friction (i.e. $\mu_s B_{o,E}$). The critical value of $\mu_s B_{o,E}$ can be employed to estimate the critical size of the particle that can exhibit capillary-driven sliding motion.

S11 Particle critical radius

Particle critical radius is the maximum particle size which can exhibit sliding motion or can be lifted up by the droplet.

Substituting the value of the equivalent Bond number in Eq. (S26) and solving for particle critical radius (Rp):

$$R_p = l_c \sqrt{\frac{3}{2\mu_s}\frac{\rho_l}{\rho_p}\tilde{F}_c} \tag{S27}$$

where ρ_l, ρ_p, $\tilde{F}_c$, l_c are liquid density, particle density, net capillary force (normalized with $2\pi R_p \sigma_l$) and capillary length ($l_c = \sqrt{\sigma_l / g\rho_l}$) respectively.

For uplifting motion, net capillary force should be higher than the component of particle weight in the direction of uplifting motion as given by the following expression:

$$Fc > W_p \cos(\pi - \beta_d) \tag{S28}$$

where W_p and β_d, are particle weight and dynamic contact angle of the air-liquid-substrate contact line, respectively. Based on the criterion given by Eq. (S28), the critical radius for particle uplifting can be determined as:

$$R_p = l_c \sqrt{\frac{3}{2\cos(\pi - \beta_d)}\frac{\rho_l}{\rho_p}\tilde{F}_c} \tag{S29}$$

Eq. (S27) and Eq. (S29) can be combined into a single expression given by Eq. (S30):

$$R_p = l_c \sqrt{\frac{3}{2}\frac{\rho_l}{\rho_p}\tilde{F}_c\frac{1}{C}} \tag{S30}$$

The constant C in Eq. (S30) is equal to μ_s for sliding motion and equal to $\cos(\pi - \beta_d)$ for particle uplifting. The symbol μ_s represents the static friction coefficient while β_d represents the dynamic contact angle of the air-liquid-substrate contact line.

S12. Capillary dynamics of a single micro-particle

The maximum net capillary force can be determined as $F_c = 2\pi R_p \sigma_l \cos^2(\theta_d/2)$[4]. The dynamic contact angle (θ_d) depends on the velocity of the air-liquid-particle contact line as shown in Fig. 3e in the main text. Though the velocity-dependent measurements for dynamic contact angle made for flat surfaces can be employed for curved geometries (i.e. micro-particles) [5], however, these measurements may not necessarily be applicable owing to unknown three-phase contact line velocity. Therefore, the dynamic contact angle and corresponding maximum net capillary force are determined through the capillary dynamics of a single micro-particle.

In these experiments, the micro-particle moved down (in the z-direction) with a discrete step size of 5 μm (see Fig. S11). The particle was held stationary once it touched the flat stationary air-liquid interface. The particle was carefully glued to the bottom of a thin column and fixed to a micro-motorized linear stage to precisely control the particle movement. The imaging setup to study the capillary dynamics of a stationary micro-particle is the same as used for studying the capillary-driven motion of micro-particles as described in Section 3.3 in the main text. Five experiments (each with a different particle) for both soda lime glass and polyethylene micro-particles were run and average values were considered. The diameter of the particles for polyethylene particles were approximately 223 μm, 243 μm, 246 μm, 227 μm and 223 μm. Similarly, the diameters of the soda lime glass micro-particles were 374 μm, 362 μm, 355 μm, 400 μm and 370 μm, respectively.

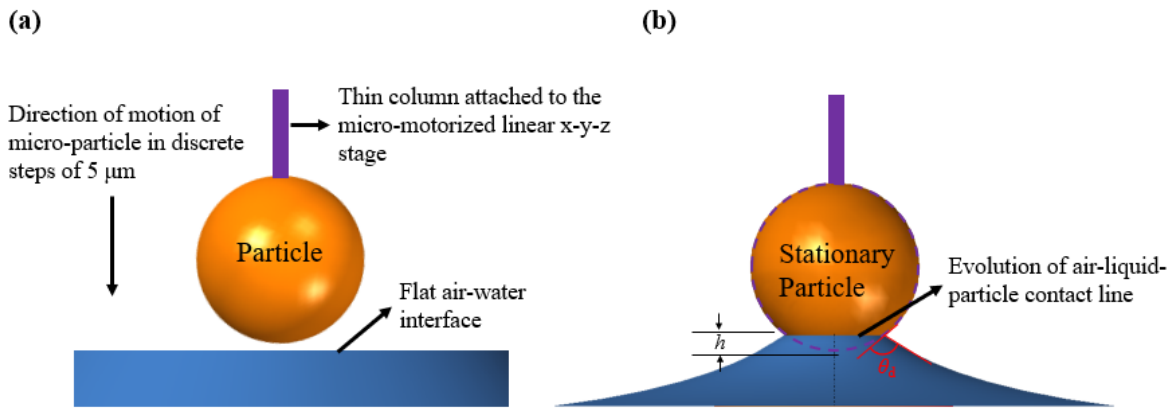

Fig. S11. Position of a particle (a) before and (b) after contacting flat air-liquid interface. The symbol θ_d in (b) represents the dynamic contact angle of the air-liquid-particle contact line.

S12.1 Role of gravity

As the growth of the air-liquid-particle contact line in this case is in an upward direction against gravity, the role of gravity needs to be carefully evaluated. The particle size for these experiments was less than 500 μm and the maximum Bond number for water is found to be 0.033. The capillary length ($l_c = \sqrt{\sigma_l / g\rho_l}$) for water is 2.7 mm. As the capillary length is significantly higher than the particle diameter (< 500 μm) and Bond number <1, interaction is assumed to have happened under a zero-gravity environment. The equilibrium height of the air-liquid-particle contact line for the soda lime glass slide can be calculated using the following equation [6].

$$h_E = \sqrt{2\frac{\sigma_l}{\rho_l g}\left(1-\sin\theta_E\right)} \tag{S31}$$

The predicted capillary height for the soda lime glass slide (with equilibrium contact angle θ_E=30) is 2.72 mm. The h_E is significantly higher than the maximum possible meniscus height which is equal to the particle diameter. Therefore, the role of gravity can be assumed negligible.

S12.2 Variation in filling and dynamic contact angle

Fig. S12a-b shows the capillary rise and growth of the air-liquid-particle contact line for soda lime glass and polyethylene micro-particles under ambient conditions (see supplementary movie #9). The variation in the dynamic contact angle and filling angle for polyethylene micro-particles is significantly smaller compared to soda lime glass micro-particles as shown in Fig. S12c. However, the polyethylene micro-particles constitute a higher dynamic contact angle compared to soda lime micro-particles at a particular filling angle. Fig. S12d shows the results for the variation of dynamic contact angle with the tangential velocity of the micro-particles. The trend clearly shows that dynamic contact angle increases with the increase in meniscus (i.e. air-liquid-particle contact line) velocity. Power law fitting of the experimental data shows that the dynamic contact angle varies with 1/4 of the velocity (u_t) of the meniscus (i.e. $\theta_d \propto u_t^{1/4}$) for soda lime glass micro-particle. However, for polyethylene micro-particle, the dynamic contact angle varies with 1/25 of the velocity (u_t) of the meniscus (i.e. $\theta_d \propto u_t^{1/25}$).

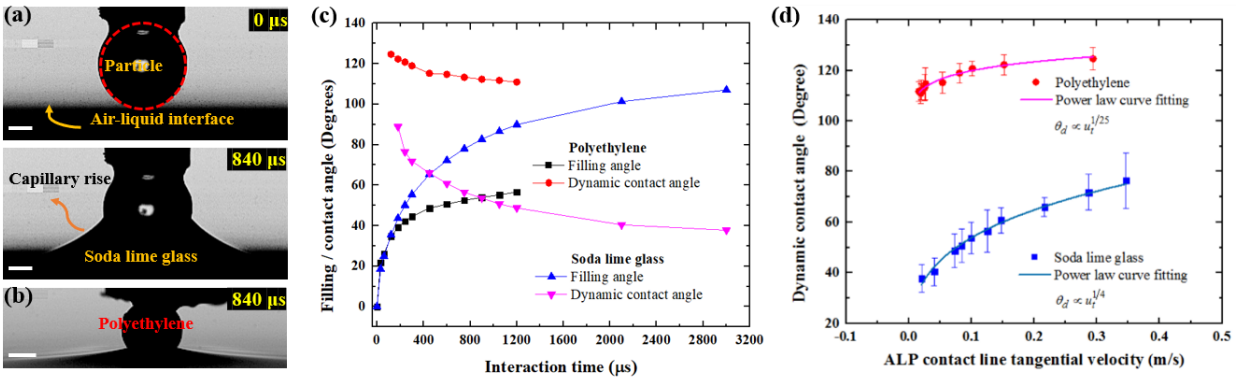

Fig. S12. Evolution of air-liquid-particle (ALP) contact line (i.e. capillary rise) during air-water interface interaction with (a) soda lime glass micro-particle with 375 μm in diameter and (b) polyethylene micro-particle with 223 μm in diameter. (Scale bar = 100 μm), (c) Variation in filling and dynamic contact angle of soda lime glass and polyethylene micro-particles with interaction time, (d) Power law curve fitting for dynamic contact angle as a function of meniscus or air-liquid-particle (ALP) contact line velocity

S12.3 Normalized capillary height and force

The normalized capillary height corresponding to maximum capillary forces is below 0.5 for both types of particles (Fig. S13). It means that the particle will not undergo capillary-driven motion once it is 50% engulfed by the advancing three-phase contact line. The net vertical capillary force, the difference between the vertical component of surface tension force and Laplace pressure force (while assuming a straight air-liquid interface at the ALP contact line), is given by Eq. S32.

$$F_c = F_{x-\sigma} - F_{LP} = \pi\sigma_l R_p \sin\phi \sin\left(\theta_d + \phi\right) \tag{S32}$$

The maximum normalized values of net capillary force in the vertical direction are 0.1 (i.e. ~2.4 μN for D_p = 100 μm) and 0.35 (i.e. ~7.9 μN for D_p = 100 μm) for polyethylene and soda lime glass micro-particles, respectively, as shown in Fig. S13. For self-cleaning, the dust particle will be difficult to remove if the adhesive resistance between particles and the contaminated surface is larger than the maximum capillary force shown in Fig. S13a. The predicted critical radii for both type of particles in sliding motion and particle lifting are shown in Fig. S13b.

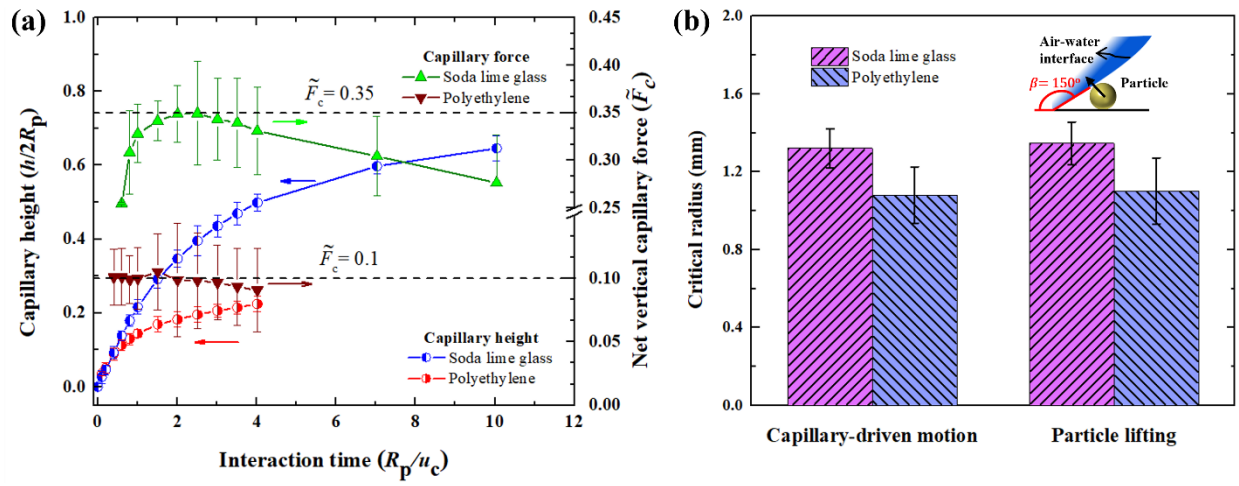

Fig. S13. (a) Variation in the vertical component of the normalized capillary force ($\tilde{F}_c = F_c / 2\pi R_p \sigma_l$) and capillary height normalized with $2R_p$ as a function of interaction time for soda lime glass and polyethylene micro-particles, respectively. (b) Predicted critical radii for soda lime glass and polyethylene particles for capillary-driven sliding motion (βd=90o) and particle uplifting (βd=150^o), respectively.

S13. Uncertainty analysis

The uncertainty analysis (where applicable) was carried out based on the approach proposed by Kline and McClintock given in [7].

S14. Description of supplementary movies

Movie #S1

Interaction of soda-lime glass micro-particle with diameters of 100 – 200 μm with an advancing ethanol meniscus captured under an optical microscope. Video playback and recording speed are 30 frames per second (fps).

Movie #S2

Infrared thermal imaging showing the top view of the air-ethanol-substrate interaction with soda lime glass micro-particles. Video playback and recording speed is 30 frames per second (fps).

Movie #S3

Top view of the air-water-substrate contact line interaction with soda lime glass micro-particle of ~245 μm in diameter. The video playback speed is 30 fps while it was captured at 33,333 fps.

Movie #S4

Side view of the air-water-substrate contact line interaction with a soda lime glass micro-particle of ~228 μm in diameter. The video playback speed is 1 fps while it was captured at 25,000 fps.

Movie #S5

Side view of the air-water-substrate contact line interaction with a soda lime glass micro-particle of ~220 μm in diameter. The video playback speed is 1 fps while it was captured at 4,200 fps.

Movie #S6

Interaction of air-water-substrate contact line with polyethylene micro-particle of ~ 230 μm in diameter. The video playback speed is 1 fps while it was captured at 25,000 fps.

Movie #S7

Lifting of soda lime glass micro-particle of ~ 331 μm in diameter by an air-water interface. The video playback speed is 1 fps while it was captured at 25,000 fps.

Movie #S8

Air-ethanol-substrate contact line interaction with soda lime glass micro-particle of ~280 μm in diameter. The video playback speed is 30 fps while it was captured at 5,000 fps.

Movie #S9

Capillary dynamics of a single soda lime glass micro-particle (370 μm in diameter). The playback speed is 10 fps while it was captured at 33,333 fps.

S15. References

[1] F. M. Orr, L. E. Scriven, and A. P. Rivas, "Pendular rings between solids: meniscus properties and capillary force," *Journal of Fluid Mechanics,* vol. 67, no. 4, pp. 723-742, 2006, doi: 10.1017/S0022112075000572.

[2] R. Clift and W. Gauvin, "The motion of particles in turbulent gas streams," *Proc.~Chemeca,* vol. 1, pp. 14-28, 01/01 1970.

[3] J. O. Bird and P. J. Chivers, "28 - Friction," in *Newnes Engineering and Physical Science Pocket Book*, J. O. Bird and P. J. Chivers Eds.: Newnes, 1993, pp. 235-237.

[4] J. Ally, M. Kappl, H.-J. Butt, and A. Amirfazli, "Detachment Force of Particles from Air−Liquid Interfaces of Films and Bubbles," *Langmuir,* vol. 26, no. 23, pp. 18135-18143, 2010/12/07 2010, doi: 10.1021/la103242e.

[5] C. W. Extrand and S. I. Moon, "Contact Angles on Spherical Surfaces," *Langmuir,* vol. 24, no. 17, pp. 9470-9473, 2008/09/02 2008, doi: 10.1021/la801091n.

[6] P.-G. de Gennes, F. Brochard-Wyart, and D. Quéré, "Capillarity and Gravity," in *Capillarity and Wetting Phenomena: Drops, Bubbles, Pearls, Waves*, P.-G. de Gennes, F. Brochard-Wyart, and D. Quéré Eds. New York, NY: Springer New York, 2004, pp. 33-67.

[7] R. J. Moffat, "Describing the uncertainties in experimental results," *Experimental Thermal and Fluid Science,* vol. 1, no. 1, pp. 3-17, 1988/01/01/ 1988, doi: https://doi.org/10.1016/0894-1777(88)90043-X.